The Astrophysical Journal, 597:590–601, 2003 November 1

SCATTERED LIGHT FROM CLOSE-IN EXTRASOLAR PLANETS: PROSPECTS OF DETECTION WITH THE *MOST* SATELLITE

Daniel Green and Jaymie Matthews
Department of Physics and Astronomy, University of British Columbia, Vancouver, BC V6T 1Z1, Canada

Sara Seager
Department of Terrestrial Magnetism, Carnegie Institution of Washington, 5241 Broad Branch Road NW, Washington, DC 20015

and

Rainer Kuschnig
Department of Physics and Astronomy, University of British Columbia, Vancouver, BC V6T 1Z1, Canada
Received 2003 January 31; accepted 2003 July 3

ABSTRACT

The ultraprecise photometric space satellite *MOST* (*Microvariability and Oscillations of STars*) will provide the first opportunity to measure the albedos and scattered light curves from known short-period extrasolar planets. Because of the changing phases of an extrasolar planet as it orbits its parent star, the combined light of the planet-star system will vary on the order of tens of micromagnitudes. The amplitude and shape of the resulting light curve is sensitive to the planet's radius and orbital inclination, as well as the composition and size distribution of the scattering particles in the planet's atmosphere. To predict the capabilities of *MOST* and other planned space missions, we have constructed a series of models of such light curves, improving upon earlier work by incorporating more realistic details such as limb darkening of the star, intrinsic granulation noise in the star itself, tidal distortion and back-heating, higher angular resolution of the light scattering from the planet, and exploration of the significance of the angular size of the star as seen from the planet. We use photometric performance simulations of the *MOST* satellite, with the light-curve models as inputs, for one of the mission's primary targets, τ Boötis. These simulations demonstrate that, even adopting a very conservative signal detection limit of 4.2 μmag in amplitude (not power), we will be able to either detect the τ Boötis planet light curve or put severe constraints on possible extrasolar planet atmospheric models.

Subject heading: planetary systems

1. INTRODUCTION

Since the discovery of a planet around 51 Peg b in 1995 (Mayor & Queloz 1995), the field of extrasolar planetary research has grown steadily. Radial velocity surveys (e.g., Marcy et al. 2003; Santos et al. 2000; Tinney et al. 2002) have found over 100 extrasolar giant planets (EGPs) orbiting nearby stars. In addition, $\sim$10 of these systems contain planets with semimajor axes $\lesssim$0.05 AU, hereafter called close-in EGPs (CEGPs). The radial velocity surveys provide the planet's minimum mass and orbital parameters (such as semimajor axis and eccentricity) but nothing else about the planet's properties. Despite the growing numbers of discoveries, we know detailed and accurate properties of only a single extrasolar planet: HD 209458b. Observations of this transiting planet HD 209458b (Charbonneau et al. 2000; Henry et al. 2000; Brown et al. 2001) have provided measurements of the radius and mean density of the planet, providing the first information on the planet's composition. Furthermore, the detection of the trace element sodium in HD 209458b's atmosphere by Charbonneau et al. (2002) has provided the first constraint on an extrasolar planet's atmosphere.

Ongoing planet transit searches (see Horne 2003) should increase the number of extrasolar planets with observed physical properties by providing a measured radius and inclination for discovered planets (see Konacki et al. 2003 for a description of the first planet detected with the transit search method). However, even for transits, little information is coming directly from the planet. For nontransiting planets, direct spectroscopy and photometry appear to be the most likely sources of additional information. Spectroscopy could reveal atmospheric composition. Ultraprecise photometry has the potential to reveal the nature of the atmospheric scattering particles: because of the changing phases of a short-period extrasolar planet as it orbits its parent star, the combined light of the planet-star system will vary on the order of tens of micromagnitudes. The shape of the resulting light curve is indicative of the atmospheric scattering particles' composition and size distribution. Unfortunately, ground-based photometry is limited by atmospheric scintillation to detect magnitude variations of 10^{-4}. Such precision is generally possible only for bright variable stars with periods of only a few minutes, such as the rapidly oscillating Ap (roAp) stars, where long-term drifts do not interfere with signal detection at high frequencies. An example of the state of the art in rapid ground-based photometry is the work of Kurtz, Dolez, & Chevreton (2003), who set a threshold of 0.2 mag in their null detection of oscillations in the Ap star HD 965. For periods of days, we know of no photometric measurements that have achieved this level of precision. The planetary light-curve amplitudes are anticipated to be below this 10^{-4} threshold. Nevertheless, planned space-based photometric telescopes are expected to detect micromagnitude variations in the next few years.

The first of these missions to go into orbit is *MOST* (*Microvariability and Oscillations of STars*), a Canadian Space Agency microsatellite housing an ultraprecise photometric instrument which was launched on 2003 June 30. *MOST* was designed to detect and characterize rapid acoustic oscillations in solar-type stars, but it also has the potential to measure the scattered light from known CEGPs. The light-curve data are sensitive to a planet's radius, inclination, and most importantly, albedo, which in turn depends on the thermal equilibrium of the planet and the composition and size range of the primary scattering particles.

MOST will not be searching stars for new planets, owing to its small aperture and limited number of accessible targets, but rather monitoring stars already known to have CEGPs, searching for scattered light signals whose periods are already well determined. The goal is to detect the scattered light signature of an extrasolar planet for the first time and to provide empirical data to test models of CEGP atmospheric composition. The *MOST* target list includes three stars with CEGPs in its first 2 years: 51 Peg, τ Boötis, and HD 209458. The photometric data will also be used to search for solar-type oscillations in the parent stars, whose eigenspectra can better refine their masses and main-sequence ages. This will also be extremely valuable in understanding the nature and history of the CEGPs themselves.

Other funded space missions—*COROT* (CNES/ESA, 2005), *Kepler* (NASA, 2007) and *Eddington* (ESA, 2007)—will monitor fields of tens of thousands of stars, discovering hundreds of new EGPs by their scattered light curves (in addition to their primary extrasolar planet goal of searching for transiting Earth-sized planets). *MOST* will provide a valuable starting point for these missions by determining the signature of the CEGP light curves that can then be used for detection algorithms and also by characterizing the low-amplitude photometric variability of solar-type stars, which will affect planet light curve and transit detections. A recent paper by Jenkins & Doyle (2003) evaluates *Kepler*'s ability to discover CEGPs by their light curves, around stars without known planets. Their paper includes an estimate of the number of planets *Kepler* expects to detect and a description of detection algorithms. Our paper is complementary, describing *MOST*'s potential for detecting CEGP light curves of *known planets* with known orbital periods.

Using a Monte Carlo method, Seager, Whitney, & Sasselov (2000) first generated scattered light curves for generic close-in EGPs to show that the resulting light curves were highly dependent on the composition and size distribution of the condensates in the atmosphere. Furthermore, Seager et al. (2000) showed that systems like 51 Peg might show light variations as large as 60 μmag peak-to-peak. Even signals 20 times smaller are expected to be within the range of detectability by *MOST* and other space missions, so these early results inspired the *MOST* team to expand their science mission to include CEGPs.

In this paper we present the results of physically more complete models of CEGP scattered light curves that include various types of noise, and we evaluate *MOST*'s capability to detect them. In § 2 we describe the planet atmosphere model and the Monte Carlo model used to produce the synthetic planet light-curve data. The stellar noise model is described in § 3, and the *MOST* performance simulation is described in § 4. In § 5 we present preliminary results and discussion of both the model and the simulated *MOST* data. We conclude the paper with a discussion of future prospects in § 6.

2. THE PLANET SCATTERED LIGHT CURVE MODEL

2.1. *The Atmosphere Structure Model*

The three-dimensional Monte Carlo model aims to compute the emergent flux at visible wavelengths from starlight that has anisotropically scattered through the planetary atmosphere. In order to compute the photons' paths through the atmosphere an input atmospheric structure is needed. For the Monte Carlo code purposes, this input atmospheric structure consists simply of the wavelength-dependent absorption and scattering coefficients as a function of location in the atmosphere. For simplicity we consider a homogeneous atmosphere, in which case only a one-dimensional radial profile (i.e., as a function of vertical atmospheric depth) of absorption and scattering coefficients is needed. (The three-dimensional Monte Carlo code is required because of highly anisotropic scattering properties of some condensate particles.) Computing the radial distribution and abundance of all of the different absorption and scattering coefficients themselves is a complex task and depends on temperature, pressure, and chemical abundances, as described below.

2.1.1. *Description of the Model Atmosphere*

The atmosphere model used here is a one-dimensional plane-parallel radiative plus convective equilibrium code. Full details are described in Seager (1999), Seager et al. (2000), and S. Seager & D. D. Sasselov (in preparation). Three parameters that describe the atmosphere are solved from three equations in a Newton-Raphson type scheme. The three parameters are temperature (as a function of depth), pressure (as a function of depth), and the radiation field (as a function of wavelength and depth). The three equations are radiative transfer, radiative+convective equilibrium, and hydrostatic equilibrium. These equations and the three parameters are highly coupled, which is why to compute the temperature-pressure structure we must also simultaneously solve for the radiation field. In order to solve the three atmosphere equations, upper and lower boundary conditions are needed. The upper boundary condition is the flux from the parent star computed with Kurucz model atmospheres (Kurucz 1992), and the lower boundary condition is the flux from the interior of the planet. We assume that the heating from irradiation is instantaneously redistributed around the tidally locked planet (but see § 2.1.2).

Beyond the equations and boundary conditions there are several other inputs to the model atmosphere code. These include planet semimajor axis and surface gravity. We adopt solar abundances to provide an easily comparable standard for future models. The choice of abundance value is a smaller uncertainty compared with cloud opacity (see the uncertainties described in § 2.1.2). In addition we do not know if the origin of Jupiter's high metallicity also applies to extrasolar planets; therefore a higher than solar metallicity is not a suitable reference point. The number density of gas and solid species comes from a Gibbs free energy chemical equilibrium calculation (described in Seager et al. 2000), which specifies the species abundance as a function of temperature and pressure. The opacities for H_2O, CH_4, Na, K, and pressure-induced H_2-H_2, H_2-He, and $MgSiO_3$ are used.

Note that H_2O is the most important gas in determining the temperature-pressure structure due to stellar irradiation. Full references for the opacities used are listed in Seager et al. (2000). Note that our more recent work (S. Seager & D. D. Sasselov, in preparation) shows that use of more recent opacities results in a similar temperature-pressure structure to the one used here (S. Seager & D. D. Sasselov, in preparation), certainly similar enough for the goal of this paper. With a self-consistent solution for the vertical temperature-pressure profile in a plane-parallel atmosphere, the absorption and scattering coefficients used in the Monte Carlo calculations come directly out of the calculation.

2.1.2. *Model Uncertainties*

Our model is relevant to first order and more than sufficient for this paper's primary goal of computing signatures of extrasolar planets with real instrumental and stellar noise concerns. Nevertheless, we must keep in mind that there are many uncertainties in the model and that any specific model can involve many choices for input parameters. Ultimately the *MOST* data will be able to constrain the large choice of parameter space and help narrow down the uncertainties.

Recent calculations of atmospheric circulation (Guillot & Showman 2002; Showman & Guillot 2002; Cho et al. 2003) have shown that the stellar irradiation acting on a close-in tidally locked gas giant planet could cause a highly nonuniform temperature distribution with horizontal temperature variations of up to 1000 K. While such atmospheric circulation models are not yet sophisticated enough to generate temperature-pressure profiles and emergent spectra, they do indicate a major uncertainty of all current CEGP atmospheric structure models that needs to be addressed in the near future. Even though the scattered light curves depend on the illuminated side only, the atmospheric circulation is still necessary to compute the atmospheric structure consistently.

There are many other uncertainties in the atmospheric models. High-temperature condensates such as $MgSiO_3$, Al_2O_3, and Fe are stable at the expected CEGP atmosphere temperatures and pressures (see, e.g., Seager et al. 2000). These high-temperature condensates form clouds, just as water ice does here on the Earth. These clouds present a major complication for EGP modeling because the strong condensate opacity is highly sensitive to the composition and size distribution of particles. The size distribution is determined by a number of physical processes that compete for grain growth and grain destruction, including condensation, coalescence, sublimation, and sedimentation. Two recently developed cloud models (Ackerman & Marley 2001; Cooper et al. 2003) aim to predict particle sizes and are meant to be used consistently in a model atmosphere that determines the temperature, pressure, and radiation field (e.g., Marley et al. 2002). Nevertheless, even these cloud models are used in homogeneous layers, not patchy clouds that may exist, and the models still have other uncertainties. We use the results of such computations as a basic guide for our choice of cloud particle size. Other uncertainties are about upper atmosphere processes such as photoionization and photochemistry, which could cause small absorptive particles.

2.1.3. *The Fiducial Atmosphere Models*

We must make choices within the large model atmosphere input parameter space; here we have chosen to work with two fiducial models. Both models have solar abundance. The first model is our cloudy model, in which we choose a vertically and horizontally homogeneous cloud of $MgSiO_3$ cloud particles that is 2 pressure-scale heights thick. Note that even though the cloud parameters are hardwired, the cloud's vertical location is self-consistently solved for according to the temperature-pressure saturated vapor pressure relation. The condensates are prescribed to have a lognormal particle size distribution having mean radii of 5 μm and $\sigma = 1.5$ μm. The phase function (i.e., the directional scattering probability) of the condensates is computed with a Mie scattering code (see Fig. 1). This silicate cloud model is motivated by considering chemistry models (see Fegley & Lodders 1996) that show $MgSiO_3$ is likely to form first as the planet cools at the expense of other Mg species. In addition, $MgSiO_3$ is likely to be the "top" cloud that the stellar photons will reach first. This is because $MgSiO_3$ is likely to be the lowest temperature condensate at the relevant CEGP temperatures.

For comparison we use a second fiducial model of a cloud-free planet where the scattering is due to Rayleigh scattering mostly from gaseous H_2. The case of no condensates on the dayside may be realized in some cases of atmospheric circulation in which condensates are transported to a much cooler nightside, where they settle out permanently from the atmosphere (Guillot & Showman 2002). For more details of the temperature-pressure profiles and the corresponding emergent spectra see S. Seager & D. D. Sasselov (in preparation).

2.2. *Monte Carlo Model*

Our Monte Carlo model is based on the methods presented in Code & Whitney (1995) and Seager et al. (2000). The overall Monte Carlo scattering problem involves following photons that come from a star, enter the planet atmosphere at a given location traveling into a given direction, scatter repeatedly in the planetary atmosphere,

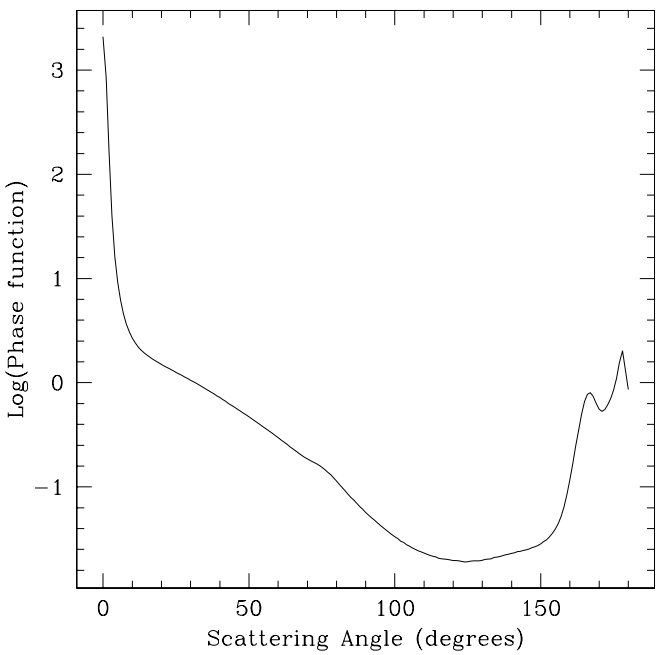

FIG. 1.—Phase function of $MgSiO_3$ at wavelength of 400.6 nm. We use a lognormal particle size distribution with mean radii of 5 μm and $\sigma = 1.5$ μm. The phase functions at other wavelengths used are not shown.

and finally exit the planet atmosphere. Essentially, probability distributions are produced for all factors involved in the photon scattering problem (e.g., initial position, distance between interactions, absorption vs. scattering) and are sampled according to

$$\xi = \int_0^a p(x)\,dx\ , \tag{1}$$

where ξ is a random number between 0 and 1, $p(x)$ is the probability density, and a is the output value. The process is repeated for each photon individually. Over 50 million photons were used in each run in order to ensure low statistical error. The final photon counts are normalized to give a ratio of the reflected flux from the planet to the flux from the star (flux ratio). One attractive feature of this method is that since each photon is independent of the last, the algorithm running time is linearly dependent on the number of photons used. Although our code lacks efficient algorithms, it is still capable of simulating large numbers of photons in relatively short periods of time.

2.2.1. *Initial Photon Properties*

Before a photon is scattered for the first time, initial characteristics of the photon are determined. The *photon wavelength* is not calculated exactly, but instead a random number determines which range of wavelengths it falls into according to the blackbody spectrum of the star. The *MOST* bandpass is close to a box function from 400 to 750 nm, and we have chosen 10 wavelength bins to represent this bandpass (based on the planet atmospheric spectrum generated in § 2.1).

The *initial coordinates and trajectory* of the photon must also be generated. The starting coordinates are produced by generating random x, y coordinates on a disk of the same radius as the planet. The EGPs with measurable scattered light curves will have semimajor axes within 0.1 AU; the stellar flux is not plane-parallel, and so the initial trajectory of the photon is nontrivial to determine. The initial trajectory of the photon is determined from the probability distribution

$$1 = k\int_0^{R_s} \frac{2}{5}\pi r\left[2 + 3\cos\left(\arcsin\frac{r}{R_s}\right)\right]dr\ , \tag{2}$$

which includes an approximation of solar limb darkening (Carroll & Ostlie 1996). In this equation, r is the radial distance on a disk of radius R_s (where R_s is the parent star radius) and k is the normalization constant. This distribution only approximates the relative amount of light incident from different directions.

2.2.2. *Photon Scattering, Absorption, and Flux*

Once the photon enters the atmosphere, it is followed through all scattering processes until it exits the atmosphere or is absorbed by a gas or solid particle. Distances between interactions are calculated separately for all types of events (scattering by gas, scattering by solids, absorption by gas, absorption by solids), and the shortest distance sampled produces an interaction. For scattering events, the new trajectory is determined by sampling the appropriate phase function (see Fig. 1 for the phase function of $MgSiO_3$).

Following these interactions, the same distance calculations are repeated until the photon is absorbed or exits the atmosphere. If absorption occurs, we assume the photon vanishes from the *MOST* bandpass; absorbed photons will be reemitted at IR wavelengths where the CEGP thermal flux peaks. Although the absorbed photons do affect the heat balance of the planet, this is already taken into account from our atmospheric structure models described in §§ 2.1.1–2.1.3. If the photon escapes the atmosphere, it is binned according to trajectory angle relative to the direction of the parent star (z-axis). This binning method assumes symmetry about the z-axis, which is reasonable for a symmetric atmosphere with symmetric illumination.

After the prespecified number of photons have been sent through the atmosphere, the photon counts are normalized to give the emergent flux. At intervals given by expected integration times for *MOST* of 1–2.5 minutes, the orbital position is calculated from the eccentricity, inclination, semimajor axis, and orientation of the orbit. From the orbital position the phase angle (the star-planet observer angle; in our case the angle between the z-axis and the observer) is calculated. The flux for the phase angle is taken from the binned data and normalized for the current distance.

2.2.3. *Planet Tidal Distortion Effects on the Light Curve*

Sinusoidal modulations in photometric light curves are observed in binary star systems with tight orbits due to tidal distortion of the stars into ellipsoidal shapes (von Zeipel 1924; Kitamura & Nakamura 1988). Even short-period (2 day) companions to solar-type primaries can cause a gravitational distortion visible on millimagnitude light curves if the companion mass is at least $\sim 0.2\ M_\odot$ (Drake 2003). We examine the same effects from a tidally distorted planet, to see whether they will affect the scattered light curve at the micromagnitude level, by estimating the distorted length of the planet's axes under the assumption of an isothermal expansion. Assuming equilibrium and cylindrical symmetry,

$$R_z = \frac{\left[\ln(g - 2g_t/g) - \left(m_{\rm H} g R_p/k_{\rm B}T\right)\right]k_{\rm B}T}{m_{\rm H}(g - 2g_t)}\ , \tag{3}$$

$$R_x = \frac{\left[\ln(g + g_t/g) - \left(m_{\rm H} g R_p/k_{\rm B}T\right)\right]k_{\rm B}T}{m_{\rm H}(g + g_t)}\ , \tag{4}$$

where R_z is the radius of the planet in the direction of the star, R_x is the perpendicular radius, and R_p is the initial spherical size of the planet. Furthermore, g is the surface gravity, $m_{\rm H}$ is the mass of hydrogen, and k_bT is the thermal energy. The tidal acceleration is $g_t = GM_sR_p/a^3$, where M_s is the stellar mass, a is the semimajor axis, and G is the gravitational constant. Given the phase angle, the relative increase or decrease in intensity is added through geometric optics instead calculating it directly in the Monte Carlo code. This approach is approximate, but given the relatively small size alterations, the impact of this assumption should be minimal. From the above equations, we found the tidal distortion to be a $\sim 10^{-7}$ effect, well below the $\sim 10^{-5}$ signal.

2.2.4. *Back-heating*

CEGPs are expected to be tidally locked because of tidal interactions between the planet and the star (Goldreich & Soter 1966; Guillot et al. 1996). The stellar atmosphere may also be affected by tidal interactions with the CEGP. Combined with the backscattering of light from the planet, the stellar atmospheres could potentially have a flux hot spot

with a rotational variation of the same period as the planet's rotational period. Although stellar back-heating is expected to be a small effect, it could be important because it would share the same period as the planetary light curve.

To investigate the magnitude of the back-heating effect we construct an approximate model, based on the results of the Monte Carlo code. From the distance between the planet and the star (it is assumed that only roughly circular orbits will produce the back-heating effect) and the angular binning used in the scattering code, several rings on the stellar surface are considered. Each stellar ring is considered to initially radiate energy according to the blackbody equation $E = A\sigma T_e^4$, where A is the emissivity, σ is the Stefan-Boltzmann constant, and T_e is the effective temperature. Using the same equation for the total flux emitted by the star, an estimate of the scattered energy is produced from the fraction of the light scattered from the planet back toward the star. Since the star must reach equilibrium between the input and expelled energy at each point on the surface, a ratio of the intensity of flux on each ring to the average can be made. Making the approximation that the flux at the planet is unchanged, we get

$$\frac{F_R(\theta)}{F_{\rm avg}} = 1 + \frac{P(\theta)}{Z}\pi R_s^2 \frac{R_p^2}{a^2}\frac{1}{A_R}\ , \qquad (5)$$

where R_s and R_p are the star and planet radius, a is the planet semimajor axis, Z is the total number of photons in the Monte Carlo code, and $P(\theta)$ is the number of photons reflecting into angle θ; A_R is the area of the ring of the stellar surface produced by binning at θ, $F_{\rm avg}$ is the initial flux of the ring, and F_R is the increased flux due to scattered light. This ratio is calculated for each ring on the stellar surface.

Once the increased stellar flux is calculated, a light curve is produced for each ring using the limb-darkening profile of the star. The profile is constructed using an approximation for solar limb darkening (Carroll & Ostlie 1996). This limb-darkening approximation has good agreement with measurements averaged over the visible spectrum. The increase in stellar flux is spatially integrated over the stellar disk for each time interval. Because of the small size of the scattered light ratio and R_p^2/a^2, our estimate shows back-heating to be a small effect (on the order of 10^{-7}) compared with the $\sim 10^{-5}$ CEGP light curve.

3. STELLAR GRANULATION NOISE

One of the fundamental limiting factors in the spectroscopic detection of extrasolar planets through Doppler shifts is the intrinsic radial velocity noise due to the changing pattern of rising granules at the top of the convection zone. The variation in filling factor and contrast of the granulation pattern is also an important noise source in ultraprecise photometry of solar-type stars.

The level of granulation noise is correlated with chromospheric activity, which in turn depends on stellar rotation rate, surface magnetic activity, and depth of the surface convection zone. The sample, selected for Doppler searches for extrasolar planets, tends to be chromospherically quiescent, so the targets for *MOST* photometry will also share that trait. However, granulation noise may still be the dominant noise source, especially at low frequencies.

Granulation noise is nonwhite, and photometry of the Sun suggests that the noise spectrum has an approximate $1/f$ dependence of amplitude on frequency (e.g., Kjeldsen & Frandsen 1992; Kjeldsen & Bedding 1998).

To simulate this noise source, we generate a grid of frequencies from zero to the Nyquist frequency appropriate to the simulated data sample. These values are inverted to create an array of $1/f$ values, then multiplied by a corresponding array of random numbers (distributed normally about zero with a variance of one) to randomize the amplitudes and phases of the components of the intrinsic noise. An inverse discrete Fourier transform on the resulting array yields a synthetic time series of granulation noise. This time series can then be multiplied by a scaling factor to match the overall level of granulation noise to be introduced.

For the Sun, photometric granulation noise at a frequency of 0.1 mHz is approximately 2 parts per million (ppm) in integrated optical broadband light (see, e.g., Kjeldsen & Bedding 1998). We have been guided by this in our simulations, since ground based photometry of other solar-type stars does not set useful upper limits on the granulation noise at relevant frequencies.

4. *MOST* AS AN ULTRAPRECISE PHOTOMETER

MOST is a small optical telescope (aperture = 15 cm; Maksutov design), with a single broadband filter (350 nm $\leq \lambda \leq$ 700 nm), feeding a CCD photometer, on board a microsatellite platform (mass = 54 kg; dimensions $60 \times 60 \times 25$ cm). The microsatellite will be stabilized to a pointing accuracy of about $\pm 10''$ by a set of miniature low-power reaction wheels designed and built by Dynacon Enterprises, Ltd., of Toronto, Canada. Although this level of attitude control outperforms (by a factor of several hundred) any existing microsatellite with such small inertia, it is still relatively poor pointing for an astronomical instrument. Hence, the *MOST* photometer is equipped with an array of Fabry microlenses to project fixed images of the entrance pupil of the telescope, illuminated by the target starlight, onto the Science CCD. Unlike a wandering image of the star, this extended Fabry image (covering about 1400 pixels) of the CCD makes the collected signal quite insensitive to the flat-field sensitivity gradients of the detector, even at the subpixel scale. For more details about technical aspects of the *MOST* experiment, see Walker et al. (2003).

MOST was launched into a low-altitude (820 km) circular polar orbit whose slight inclination will cause it to precess at the sidereal rate, so the orbital plane is synchronous with the Sun. Launch took place on board a Russian three-stage *Rockot* launch vehicle (designated an SS-19 in the West, since it is a former Soviet ICBM) from the Plesetsk Cosmodrome. It will be injected into an orbit that will keep it above the Earth's terminator. From this vantage point, the telescope will always look over the shadowed limb of the Earth, minimizing scattered Earthlight, which could interfere with the ultraprecise photometry. This orbit also provides a continuous viewing zone (CVZ) in the sky spanning declinations $+34^\circ \leq \delta \leq -18^\circ$. Stars passing through the center of this band will remain visible continuously for about 8 weeks. The *MOST* CVZ includes several prominent extrasolar planet systems, including 51 Pegasi, τ Boötis, and HD 209458, which have been included as primary science targets for the *MOST* mission.

MOST was designed to achieve the mission's primary goal of detecting rapid photometric oscillations (periods of

several minutes) in bright ($V \leq 6$) solar-type, metal-poor subdwarf and magnetic Ap stars with precisions approaching 1 ppm (1 μmag). Although *MOST* is a *non*differential photometer, the relatively high frequencies of the periodic oscillations can be clearly distinguished in a Fourier spectrum of the data from the lower frequency modulations, drifts, and noise (e.g., orbital variations with $P_{\rm orb} \simeq 100$ minutes; granulation noise in the stars themselves).

This is not true for the periodic reflected light signals from extrasolar planets, whose orbital frequencies ($\nu_{\rm orbit} \simeq 0.2$–$0.3$ day$^{-1} \simeq 0.003$ mHz) are very low compared with the intended sensitivity range of *MOST* ($\nu_{\rm osc} \simeq 0.5$–6 mHz). Therefore, *MOST* nondifferential photometry of extrasolar planet systems will be more prone to the long-term drifts and modulations. If *MOST* were intended to be a planet *hunter*, searching this low-frequency regime for unknown periodic signals in a noisy background, this might be a fatal flaw. However, as a probe of known extrasolar planet systems whose periods have already been specified accurately from radial velocity data, *MOST* can be quite effective, as we will demonstrate in § 5.

4.1. *Modeling the Photometric Performance of MOST*

MOST is optimized to collect very precise photometry for stars in the magnitude range $0.0 \leq V \leq 6.0$, with integration times from about 0.2 to 60 s, depending on the flux of the target. For extrasolar planet photometry, the integration time would be set to bring the total signal per exposure to about 80% of the full-well potential of each CCD pixel, maximizing the signal-to-noise ratio (S/N) without sacrificing linearity. For a star of magnitude $V = 0$, *MOST* would collect approximately 1.6×10^8 electrons s^{-1}, although to avoid saturation on such a bright target, the integration time would have to be about 0.2 s. For extrasolar planet targets with long periods (compared with the rapid stellar oscillations), fast time sampling is not a consideration, so every exposure can be long enough to guarantee a maximum S/N of about 220 per pixel per exposure, hence an S/N of about 8300 over the entire 1400 pixel Fabry image. Further improvements in S/N are possible by substantially binning these short exposures. With extrasolar planet orbital periods of several days, 60 s exposures can safely be binned in groups of several hundred without appreciably losing resolution in orbital phase.

As part of the design and testing process for the *MOST* mission, a comprehensive simulator of *MOST* photometry was developed, written in IDL (Kuschnig et al. 2003). This simulation code was designed to include as many noise, drift, and modulation effects as could be anticipated and modeled by the *MOST* Instrument and Science Teams. The effects can be grouped into four categories: (1) intrinsic variations and noise from the target star (and planet), (2) orbit and radiation environment, (3) sky background and attitude control errors, and (4) detector and electronics. These will be discussed in more detail by R. Kuschnig et al., in preparation, but are summarized in the next few paragraphs.

1. *Effects intrinsic to the target star+planet*.—These include the Poisson noise associated with the total flux from the system, photometric noise associated with granulation in the star's photosphere, rotational modulation due to starspots, and the periodic variations in scattered light from the planet. The last three are included in the extrasolar planet light-curve model (see § 2), although they can also be introduced by the *MOST* photometry simulator independently.

2. *Orbit and radiation environment*.—*MOST* orbits the Earth approximately every 101 minutes; the exact period will be known very accurately after launch and final orbital injection. Although from its vantage point above the terminator, *MOST* will only see the nightside limb of the Earth in normal operation, it is possible that there will be some contamination due to stray light scattered from the Earth, varying with *MOST*'s orbital period. It is possible to add stray light at a level consistent with albedo models of the Earth (e.g., Shaw, Merle, & Wilson 1998; Buzasi 2002). The fluxes of high-energy protons and electrons have been calculated for the *MOST* orbit, and cosmic-ray hits onto the Science CCD based on these fluxes have been included in the simulations. Also, *MOST* will pass through the South Atlantic Anomaly (SAA), exposing it to much higher particle fluxes for several minutes on some orbits. Rather than try to extract photometry from the CCD during these brief passages, we have conservatively not included these data in the time series, introducing short nonperiodic gaps that have only a modest effect on the window function of the Fourier spectrum. The CCDs are temperature-stabilized by a passive thermal control system that maintains the operating temperature at about -40.0 ± 0.1 °C. However, we have anticipated there might be a subtle modulation in temperature of 0.1 °C (the level of control of the CCD thermal control system) at the *MOST* orbit period and have included that effect on the CCD output.

3. *Sky background and attitude control errors*.—The *MOST* photometry is obtained through a diaphragm 1′ in diameter, which will include a sky background of zodiacal light, atomic oxygen glow (even at 820 km altitude), stray Earthlight (already modeled in category 2), scattered light from off-axis sources, and faint stars and galaxies adjacent to the target in the sky. The *MOST* Telescope and Camera are equipped with a series of baffles designed to reduce parasitic stray light by a factor of 10^{-12}, but we conservatively include a variable sky background. Wander in telescope pointing due to attitude control errors of about $\pm 10''$ has several effects: (*a*) The target starlight beam wanders across the surface of the Fabry lens, which produces the pupil image, subtly changing the ray paths within the glass and possibly encountering contaminants on different parts of the lens surface. (*b*) Faint stars or galaxies near the edge of the diaphragm can wander in and out of the field, varying the sky background level. (*c*) The pupil image will not be completely fixed, although the image motion will only be at a level of about 0.1 pixel in the *MOST* focal plane. The attitude control system (ACS) errors are modeled based on simulations of the satellite pointing performance. These models are used to introduce errors due to the target starbeam wander (effect *a*). Effect *b* is negligible for the bright targets we consider here, unless a background star is within about 8 mag of the target star brightness. We have investigated all the target fields—including the extrasolar planet fields—and there are no potentially worrisome neighbors in any field. Effect *c* is negligible because of the large size of the pupil image on the CCD, so even subpixel sensitivity variations of a few times 10% do not manifest themselves in the pupil image motion.

4. *Detector and electronics*.—These effects include (*a*) CCD readout noise, (*b*) dark noise and possible drifts in dark current, (*c*) pixel-to-pixel and subpixel sensitivity

gradients (see category 3 above), (*d*) analog-to-digital conversion (ADC) nonlinearities, (*e*) slight variations in readout-channel gain, and (*f*) uncertainties in the integration times.

In our simulations, by far the dominant sources of noise are Poisson statistics (photon noise) and stellar granulation. The photon noise in the τ Boötis simulations shown in § 5 is at a level of 0.74 ppm (1 σ). If granulation noise is included in the simulations, the 1 σ noise rises to 1.40 ppm. The other noise sources turn out to be negligible for the timescales associated with CEGP scattered light curves. However, for a more detailed breakdown of the photometric error budget of *MOST*, see Tables 5 and 6 in Walker et al. (2003).

5. RESULTS

5.1. *Simulations of Scattered Light Curves*

One of the most important aspects of our model is that it takes into account the angular size of the star as seen from the planet. We have found that using an extended source with limb darkening, the shape of the resulting light curve is significantly altered (see Fig. 2) compared with a point source. With a point source, the detailed, high angular resolution features of the phase function of scatterers remain apparent at planet-star separations $\gtrsim$0.07 AU. This effect had gone unnoticed in previous simulations (Seager et al. 2000) because of the low angular resolution used to calculate the fluxes scattered from the planet in those models. Our work has shown that it is essential to use angular bins of less than a degree to properly compute the light curves, especially for the very close-in extrasolar planets. With the proper source geometry, these features are smoothed for separations smaller than 0.07 AU and the amplitude of the light curve is reduced by up to 20% for orbital inclinations near 90° (as noted in Seager et al. 2000).

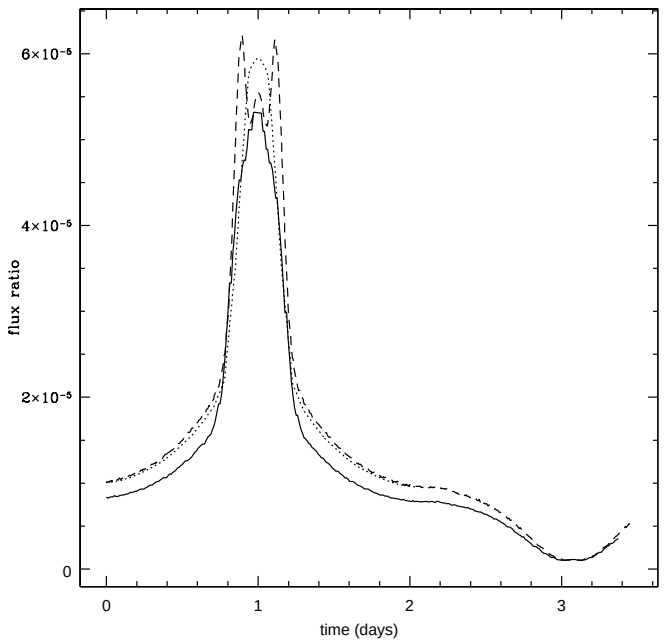

FIG. 2.—Simulated scattered light curve of τ Boötis. The flux ratio is given by the ratio between the reflected flux of the planet and flux from the star. The different lines are for different parent star assumptions: a limb-darkened sphere with 0°.5 binning (*solid line*; the limb darkening is a model consistent with measurements averaged over the visible spectrum), a point source (*dashed line*) with 0°.5 binning, and a point source with 6° binning in the light curve (*dotted line*). Note that the features in the light curve near time = 1 day when a point source (i.e., plane-parallel light rays) with 0°.5 binning is used.

The addition of stellar back-heating was found to be negligible even for space-based photometry of precision 1 ppm. Typically, stellar back-heating contributed a flux ratio of 10^{-7} or less. The effect of tidal distortion was slightly larger than back-heating. The tidal distortion alone can change the scattered flux of a planet at 0.045 AU from 0.9956 at minimum projected area to 1.0022 at maximum area, where 1.0 is the undistorted value. This translates to an additional variation of 5×10^{-7} about the mean in the light curve. Although treatment of both these effects was approximate, our initial estimates suggest that their influences will not be detectable in *MOST* observations of extrasolar planets. However, they could be important diagnostics in data from later space missions like *Kepler* and *Eddington* with improved sensitivity and long-term stability. Therefore, we have retained these effects in our models.

Given that the orbital inclinations, radii, and atmospheric structure and compositions are unknown for most extrasolar planets, it is important to understand how the planet scattered light curve varies with these parameters. Here we explore parameter variation for a fixed atmosphere model. The amplitude of the light curve is highly dependent on the inclination. As shown in Figure 3*a*, the peak value can drop by up to an order of magnitude when the inclination is changed from 90° to 50°. Seager et al. (2000) have studied this effect, which will be very important when considering possible detection of these light curves. The radius, as one might expect, makes a large contribution to the amplitude of the light curve. Over a small range of possible planetary radii, the amplitude at all points varies proportionally to the radius squared (Fig 3*c*). By comparing the effects of inclination and radius (Figs. 3*b* and 3*c*), the shape of the curve is altered in a unique way for each parameter (given a specific atmospheric model). From Figure 3, the inclination clearly distorts the light-curve shape while the radius simply scales the amplitude. The overall shape and reflective properties of the planet light curve are highly dependent on the presence of clouds in the atmosphere (Fig. 4 and also see § 2).

A change in the planet's semimajor axis would change the amplitude of the scattered light curve by a factor of $1/a^2$. However, a different semimajor axis will also change the shape of the light curve (Fig. 3*b*). As the semimajor axis increases, the angular size of the star as viewed from the planet decreases. As a result, beyond 0.07 AU distinct features of the phase function become visible because they are not "washed out" by multidirectional photon trajectories (see Fig. 2).

Our model does allow for changes in the incident flux and angular size of the star as seen from the planet in the case of a noncircular orbit. However, modeling the change in the planet atmosphere as a function of its changing temperature in an eccentric orbit is much more complicated. Such temperature variations will also affect the photon wavelength distribution and the level of tidal distortion. However, only close-in extrasolar planet systems with nearly circular orbits have been selected as *MOST* primary targets, so the current assumptions of zero eccentricity are valid.

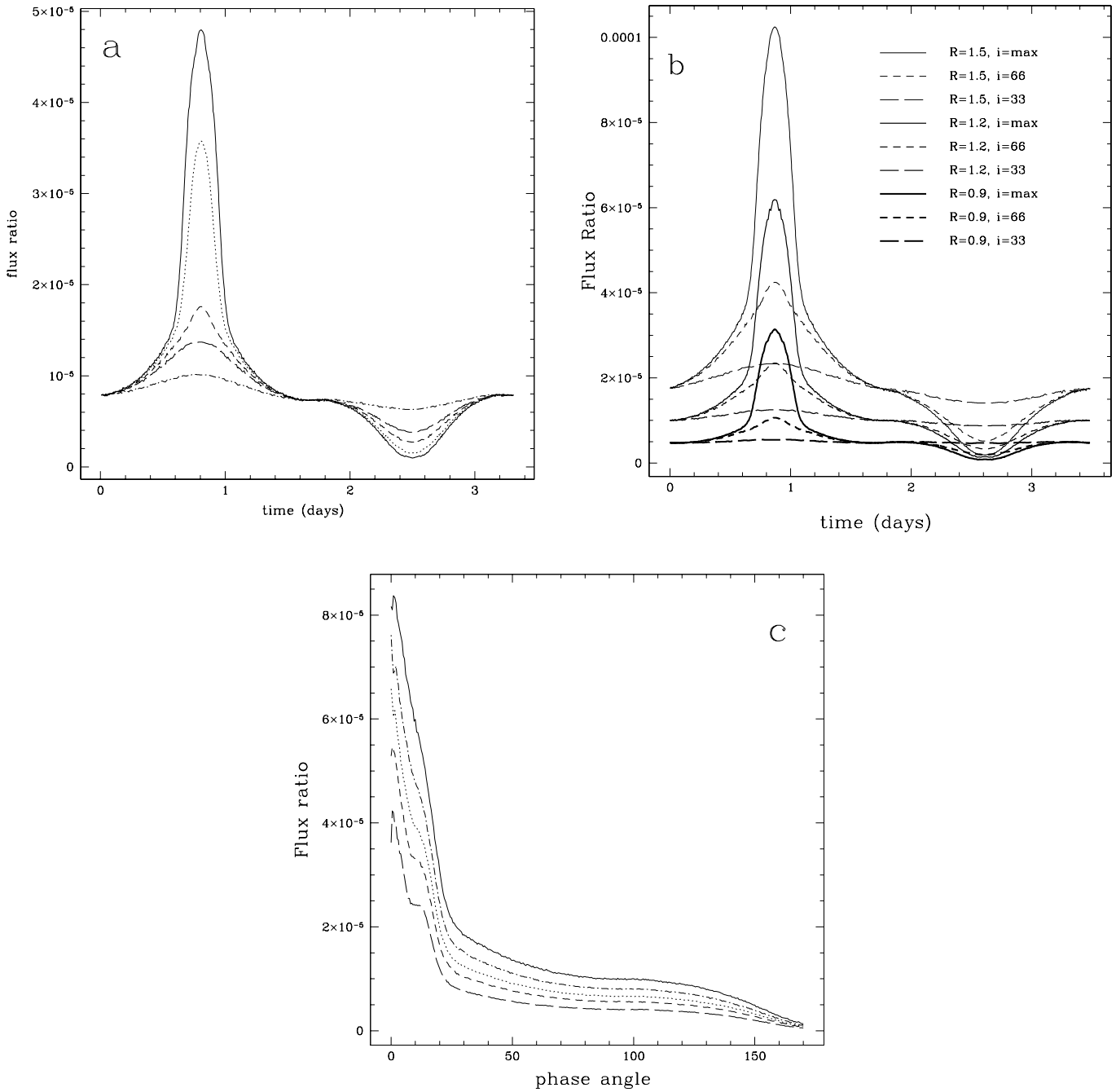

FIG. 3.—Effects of changing the inclination, semimajor axis, and planet radius on the planet light curve for our fiducial model atmosphere. (*a*) Effects of inclination on our τ Boötis model at 0.035 AU and with $R_p = 1.3R_J$. The different inclinations shown are 30° (*long-dash–dotted line*), 50° (*short-dash–dot line*), 67° (*long-dashed line*), 75° (*short-dashed line*), and 80° (*dotted line*), as well as the maximum before transit (*solid line*), 85°. (*b*) The effects of changing R_p and inclination for a model planet at 0.045 AU. The planet radius is $1.5R_J$ (*top set of curves*), $1.2R_J$ (*middle set of curves*), and $0.9R_J$ (*bottom set of curves*), and inclinations of maximum before transit (*solid line*) 66° (*dotted line*), and 33° (*dashed line*). Note that the planet atmosphere model was not changed to account for the different R_p. (*c*) Effects of different semimajor axes on our τ Boötis model of $1.3R_J$ at maximum inclination before transit. The semimajor axes are 0.045 AU (*solid line*), 0.05 AU (*dotted line*), 0.06 AU (*short-dashed line*), and 0.07 AU (*long-dashed line*). Note that the planet atmosphere model was not changed to account for the different semimajor axes and parent star irradiation. (Panel *c* is shown as a function of phase angle so that the light curves of different periods can be put on the same scale.)

5.2. *Simulations of MOST Photometry of Extrasolar Planets*

The outputs of the extrasolar planet light-curve model described in §§ 2 and 3 were used as the inputs to the *MOST* photometric simulation program described in § 5.2. The light-curve model gives the intrinsic variability of the (star+planet) system as seen from above the Earth's atmosphere, while the photometric simulation adds realistic noise and variability inherent to the *MOST* instrument. Three different inclinations of the planet orbit have been considered: $i = 33°$, $i = 67°$, and $i \sim 90°$ (more accurately, the maximum inclination that does not produce transits, since transits have not been observed in τ Boötis or 51 Peg).

For this paper, we present synthetic data for one of the prime extrasolar planet targets for the *MOST* mission:

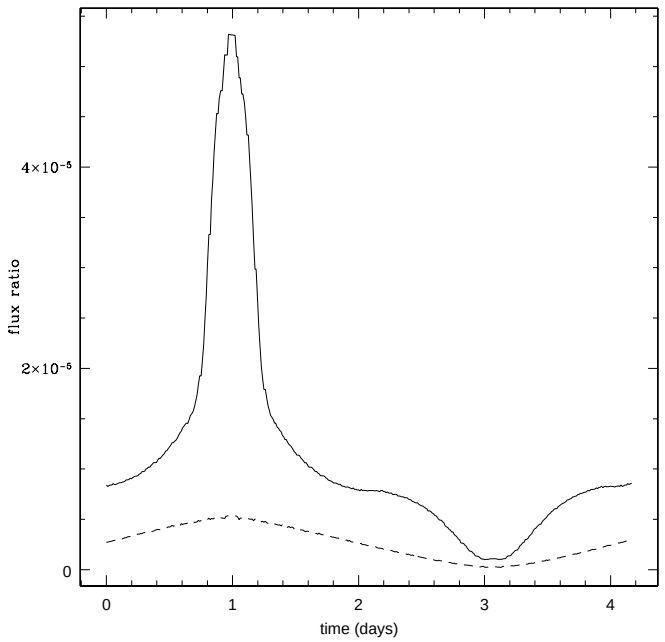

FIG. 4.—Model planet at 0.05 AU and $R_p = 1.3R_J$ is shown with (*solid line*) and without (*dashed line*) a cloud layer.

τ Boötis b. The star τ Boötis can be observed by *MOST* for about 50 days without interruption (except for brief passages through the SAA; see § 4.1), so the synthetic data set spans this time interval. The integration time for each exposure is 24 s.

The reduction of the synthetic data has been fairly simple and conservative, deliberately avoiding any calibrations that could be influenced by our foreknowledge of the input. Mean bias values have been subtracted from all the measurements. Exposures obviously affected by cosmic-ray strikes, and those collected during spacecraft passage through the SAA, have been discarded. The synthetic data are then binned to produce a net time sampling of 100 minutes (the orbital period of *MOST*) to average out any periodic variations in stray light and temperature due to orbital modulation. In these simulations, we have adopted a granulation noise amplitude and spectrum comparable to the Sun (see § 3).

The simulated photometry for τ Boötis observed at an orbital inclination of $i = 67°$ is presented in Figure 5, showing the unbinned data (*filled symbols*) and the same data binned into groups of 100 minutes each (*open symbols*). The modulation of the flux due to the extrasolar planet orbit orbital period is just barely discernible by eye in the data presented in this form. The periodic modulation becomes more obvious in Figure 6, where those data have been binned in phase according to the known orbital period of τ Boötis b. Also shown in this figure are the original input models for the three different inclinations modeled. The binned data clearly follow the input model appropriate for this data set.

5.3. *Harmonic Structure of the Light Curves*

The detection and characterization of the planet scattered light variation is even more obvious in Fourier space. In Figure 7 we show Fourier amplitude spectra of the time series presented in Figures 5 and 6, plotted out to a frequency of 0.03 mHz. The Nyquist frequency of the sample is 0.08 mHz, but there are neither spectral window artifacts nor increased noise at higher frequencies. The inset in Figure 7 shows the spectral window function, demonstrating that the *MOST* data sampling does not introduce any serious aliasing. These data contain intrinsic stellar

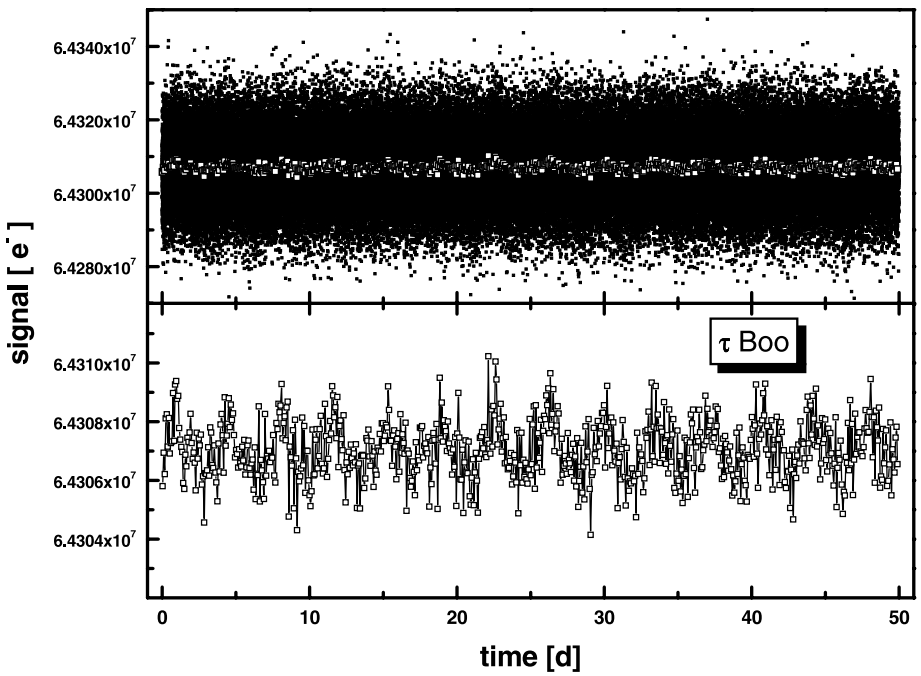

FIG. 5.—Simulated *MOST* photometry of τ Boötis, 67° inclination model, time base 50 days. *Top:* Signal in e^- for 25 s integrations (data collected in the SAA or affected by cosmic rays have been rejected; *small black squares*) and mean signal e^- data binned over the spacecraft orbit period of 100 minutes (*open squares*). The bottom panel is an expanded view of the binned data.

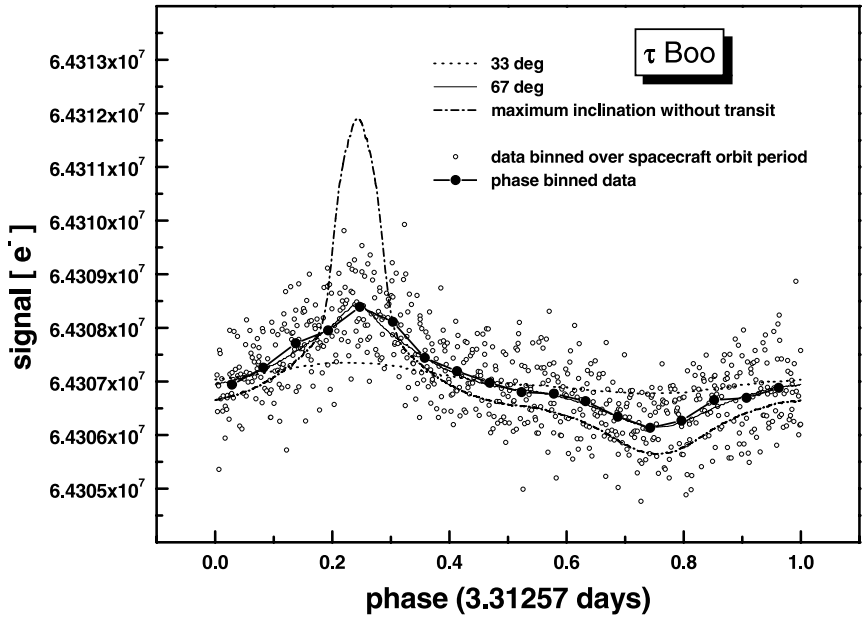

FIG. 6.—Signals of τ Boötis model (67° inclination) photometry vs. phase of the planet's orbital period. The open circles represent the binned data, and the connected black circles are the mean photometric signals for each (0.05) phase interval. The light curve for the three models are shown as well: the dotted line is for 33°, the solid line is for 67°, and the dash-dotted line is for the maximum inclination before transit.

granulation noise with a $1/f$ frequency dependence, which is principally evident starting at frequencies below 0.003 mHz.

The fundamental peak and characteristic harmonics in Fourier space make even the low-amplitude periodic signals easier to recognize. However, Figure 7 also shows that the Fourier spectrum of the photometry is a valuable way to objectively describe the detailed shape of the light curve. The spectrum of the simulated *MOST* data is plotted as the bold curve, while the three representative input simulations of the planet light curves are lighter lines. The *MOST* "data" and the 67° inclination model to which it corresponds lie on top of one another. Note also that the harmonic structure of the light curves is very sensitive to the inclination. The amplitude ratio of the first harmonic to fundamental drops noticeably with decreasing inclination compared with higher harmonics.

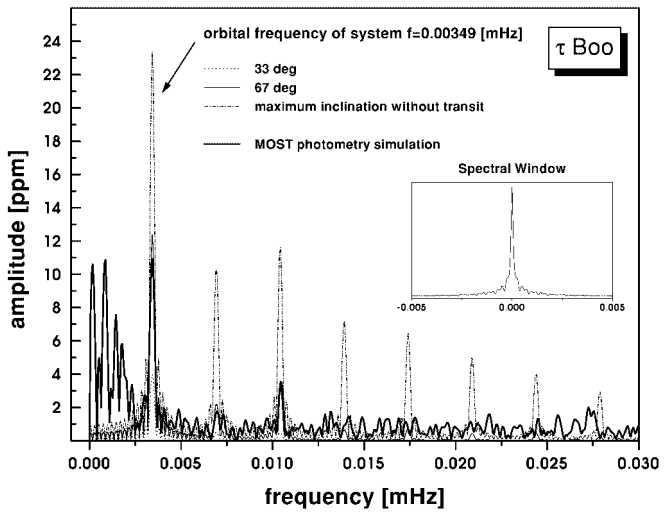

FIG. 7.—Amplitude spectra of a τ Boötis model (67° inclination), photon, instrumental, and granulation noise, and combination of these. In addition, the spectral window is shown (*inset*). The Fourier analysis of the noise has been applied to the binned data with a time base of 50 days.

To investigate this further, we generated a more complete grid of models sampling orbital inclination i, for two planet radii (1.1 and 1.5 Jupiter radii [R_J]), and plotted the fundamental and harmonic peak amplitudes as a function of orbital inclination i (Fig. 8). This figure also quantifies our ability to detect light variations for various inclinations and radii (for our fixed fiducial model atmosphere). We show in Figure 8 a very conservative detection limit of 4.2 ppm; this is 3 times the mean noise level, corresponding to about 99.7% confidence. We emphasize that the detection threshold given in Figure 8 is extremely conservative, based on the detection of signal peaks in amplitude (not power) whose frequencies are not known a priori. In a power spectrum, the S/N evident in Figure 8 would be squared, but we prefer to present amplitude spectra to err on the side of caution. Also, we will know in advance the frequencies of the fundamental orbital period and its harmonics, so the standard 3 σ detection limit is a severe overestimate. Figure 8 suggests that planetary reflected light signals should be detectable even at relatively modest orbital inclinations.

The harmonic amplitudes have different dependences on inclination and radius, which will be valuable in finding the correct match between model and data. The "forward" approach of adjusting the model to fit the observations is not efficient and may lead to close but incorrect matches. By comparing the harmonic content of the data to those of models from a grid of extrasolar planet parameters, we can eliminate obvious mismatches and narrow the search to the most promising candidate models more quickly and reliably. This approach is already widely used in the pulsating star community, where Fourier decomposition of δ Scuti light curves has become a valuable tool in identifying

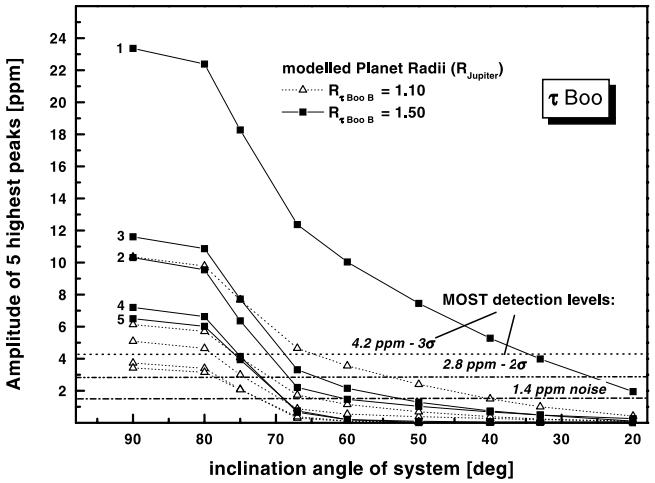

FIG. 8.—Amplitude of the five highest Fourier peaks as a function of orbital inclination (corresponding to the fundamental and the four lowest harmonics relative to the fundamental) for the τ Boötis amplitude spectrum shown in Fig. 7. The horizontal lines (*bottom to top*) show the mean noise level and the 2 and 3 σ detection limits. (Note that in the power spectrum, as opposed to this amplitude spectrum, the S/N will be squared.)

nonradial modes in those pulsators (e.g., Poretti 2001 and references therein). We are exploring the diagnostic potential of Fourier decomposition for extrasolar planet light curves, including the underlying physics that affect the light-curve shapes, and will present this work in a subsequent paper.

6. DISCUSSION AND CONCLUSIONS

The first detection and measurements (even of moderate S/N) of CEGP light curves will significantly advance our understanding of these planets. *MOST* will be the first instrument with the photometric precision to tackle this task. To demonstrate *MOST*'s exciting potential, we have run a series of simulations for a specific fiducial atmospheric model of the planet τ Boötis b (described in § 2). Other atmosphere models will result in different light-curve shapes and amplitudes; however, the condensate size distribution that we have adopted is plausible for a quiescent atmosphere (Ackerman & Marley 2001; Cooper et al. 2003). The parameter space of CEGP atmospheric unknowns is so large at present (see § 2.1.2) that a full exploration is beyond the scope of this initial study. *MOST* will soon return real data, either measuring the albedo and the CEGP light-curve shape or setting a meaningful upper limit. This will greatly narrow the allowed range of parameter space of atmospheric models.

Using our fiducial model for τ Boötis b, orbiting with a period of about 3.3 days, we have shown that *MOST*'s conservative threshold for detection of a light variation is about 2.5 ppm, with binned data taken over 50 days. This estimate includes realistic models of both stellar granulation noise and of *MOST*'s noise environment. Such a low limit means we have a good chance to measure the planet light curve even if the atmosphere differs from our fiducial model. Furthermore, *MOST* should detect the CEGPs across a relatively broad range of orbital inclinations. The Fourier amplitude spectrum of the data will be particularly sensitive to the signal and the detailed shape of its light curve.

Because the actual light-curve shape (and hence dominant scattering particle type) is unknown a priori, we will need to fit many different atmosphere models with different radii and inclinations to the real data. Although from our simulations we can recover the fiducial input model, including the planet radius and inclination, there is little point specifying the accuracy of such a recovery; with real data the goal is to detect and measure the shape of the light curve to constrain the atmosphere model, radius, and inclination. Although this work indicates that the degeneracy between planet light curve, radius, and inclination should not be severe, more work is needed to explore this for a variety of atmosphere models.

The case of HD 209458b offers a unique opportunity to determine the atmospheric composition because the planet's radius and inclination are already known from fits to the transit light curve. A measurement of the secondary transit would give the albedo at a known phase angle and radius. In addition, the shape of the light curve will aid us first in determining a light-curve signature to be used in detection of light curves from planets with non–edge-on inclinations and then in progressing toward a workable model of the atmosphere. We are currently working on simulations of HD 209458b.

In modeling CEGP light curves we have made several improvements and extensions upon previous work. One significant point is that the angular size of the star is important for planets with semimajor axes less than 0.1 AU. This affects the high angular resolution features of the light curve compared with using a point-source star (see Figure 2). In addition, modeling the light curve with a star of finite angular size instead of a point source causes a reduction in amplitude of a highly backscattering-peaked light curve by approximately 20% (as first noted in Seager et al. 2000). The other new effects that we investigated, tidal distortion of the planet and stellar back-heating, were found to have a negligible effect on the planet light curve at the level of sensitivity of the *MOST* instrument but may be important for subsequent space missions.

The results of this paper strongly suggest that *MOST* will be able to detect the τ Boötis planet light curve. Even a null result on this star and the other CEGPs in the *MOST* target list—given that the ultrahigh photometric precision attainable—would eliminate a vast range of extrasolar planet atmosphere models with medium to high albedos.

REFERENCES

Ackerman, A. S., & Marley, M. S. 2001, ApJ, 556, 872
Brown, T., Charbonneau, D., Gilliland, R., Noyes, R. W., & Burrows, A. 2001, ApJ, 552, 699
Buzasi, D. L. 2000, in Third MONS Workshop: Science Preparation and Target Selection, ed. T. C. Teixeira & T. R. Bedding (Aarhus: Aarhus Univ.), 9
Carroll, B., & Ostlie, D. 1996, An Introduction to Modern Astrophysics (Reading: Addison)
Charbonneau, D., Brown, T., Latham, D., & Mayor, M. 2000, ApJ, 529, L45
Charbonneau, D., Brown, T., Noyes, R. W., & Gilliland, R. 2002, ApJ, 568, 377
Cho, J. Y.-K., Menou, K., Hansen, B., & Seager, S. 2003, ApJ, 587, L117
Code, A., & Whitney, B. 1995, ApJ, 441, 400
Cooper, C. S., Sudarsky, D., Milsom, J. A., Lunine, J. I., & Burrows, A. 2003, ApJ, 586, 1320

Drake, A. J. 2003, ApJ, 89, 1020
Fegley, B., & Lodders, K. 1996, ApJ, 472, L37
Goldreich, P., & Soter, S. 1966, Icarus, 5, 375
Guillot, T., Burrows, A., Hubbard, W. B., Lunine, J. I., & Saumon, D. 1996, ApJ, 459, L35
Guillot, T., & Showman, A. 2002, A&A, 385, 156
Henry, G., Marcy, G., Butler, P., & Vogt, S. 2000, ApJ, 529, L41
Horne, K. 2003, in ASP Conf. Ser. 294, Scientific Frontiers in Research on Extrasolar Planets, ed. D. Deming & S. Seager (San Francisco: ASP)
Jenkins, J. M., & Doyle, L. R. 2003, ApJ, 595, 429
Kitamura, M., & Nakamura, Y. 1988, Ap&SS, 145, 117
Kjeldsen, H., & Bedding, T. 1998, in Proc. First MONS Workshop (Aarhus: Aarhus Univ.), 1
Kjeldsen, H., & Frandsen, S. 1992, PASP, 104, 413
Konacki, M., Torres, G., Jha, S., & Sasselov, D. 2003, Nature, 421, 507
Kurtz, D. W., Dolez, N., & Chevreton, M. 2003, A&A, 398, 1117
Kurucz, R. 1992, in IAU Symp. 159, Stellar Population of Galaxies, ed. B. Barbuy & A. Renzini (Dorderecht: Kluwer), 225
Marcy, G., Butler, P., Fisher, D., & Vogt, S. 2003, ASP Conf. Ser. 294, Scientific Frontiers in Research on Extrasolar Planets, ed. D. Deming & S. Seager (San Francisco: ASP)
Marley, M. S., Seager, S., Saumon, D., Lodders, K., Ackerman, A. S., Freedman, R. S., & Fan, X. 2002, ApJ, 568, 335
Mayor, M., & Queloz, D. 1995, Nature, 378, 355
Poretti, E. 2001, A&A, 371, 986
Santos, N. C., Mayor, M., Naef, D., Pepe, F., Queloz, D., Udry, S., & Blecha, A. 2000, A&A, 361, 265
Seager, S. 1999, Ph.D. thesis (Harvard Univ.)
Seager, S., Whitney, B., & Sasselov, D. D. 2000, ApJ, 540, 504
Shaw, D., Merle, R., & Wilson, J. 1998, Scattered Light from the Earth Limb Measured with the STIS CCD (STIS Instrum. Sci. Rep. 98-21)
Showman, A., & Guillot, T. 2002, A&A, 385, 166
Tinney, C., Butler, P., Marcy, G., Jones, H., Penny, A., McCarthy, C., & Carter, B. 2002, ApJ, 571, 528
von Zeipel, H. 1924, MNRAS, 84, 665
Walker, G. A. H., et al. 2003, PASP, 115, 1023